Constraining the reionization history using deep learning from 21-cm tomography with the Square Kilometre Array

Tumelo Mangena [1,2]★ Sultan Hassan [1,3]★† and Mario G. Santos[1,2]

[1]*Department of Physics and Astronomy, University of the Western Cape, Bellville, Cape Town 7535, South Africa*
[2]*South African Radio Astronomy Observatory (SARAO), 2 Fir Street, Observatory, Cape Town 7925, South Africa*
[3]*Department of Astronomy, New Mexico State University, Las Cruces NM 88003, USA*

ABSTRACT

Upcoming 21-cm surveys with the SKA1-LOW telescope will enable imaging of the neutral hydrogen distribution on cosmological scales in the early Universe. These surveys are expected to generate huge imaging data sets that will encode more information than the power spectrum. This provides an alternative unique way to constrain the reionization history, which might break the degeneracy in the power spectral analysis. Using convolutional neural networks, we create a fast estimator of the neutral fraction from the 21-cm maps that are produced by our large seminumerical simulation. Our estimator is able to efficiently recover the neutral fraction (x_{HI}) at several redshifts with a high accuracy of 99 per cent as quantified by the coefficient of determination R^2. Adding the instrumental effects from the SKA design slightly increases the loss function, but nevertheless we are still able to recover the neutral fraction with a similar high accuracy of 98 per cent, which is only 1 per cent less. While a weak dependence on redshift is observed, the accuracy increases rapidly with decreasing neutral fraction. This is due to the fact that the instrumental noise increases towards high redshift where the Universe is highly neutral. Our results show the promise of directly using 21cm-tomography to constrain the reionization history in a model-independent way, complementing similar efforts, such as those of the optical depth measurements from the cosmic microwave background observations by *Planck*.

Key words: cosmology: early Universe – cosmology: dark ages, reionization, first stars – ISM:HII regions – (galaxies:) intergalactic medium.

1 INTRODUCTION

The epoch of reionization (EoR) marks a period in the early Universe during which the birth of the first luminous cosmic structures gradually reionized the Intergalactic medium (IGM). The EoR contains enormous cosmological and astrophysical information that is important to understand galaxy evolution and formation Loeb & Barkana (2001).

However, the history of reionization remains quite unconstrained. Lyman-α forest observations at z~6 have placed upper limits on the IGM neutral fraction, which indicates that the Universe was nearly ionized by these epochs, $x_{HI} \leq 0.01$ (Fan, Carilli & Keating 2006; Becker et al. 2015). Using identified Ly α emitters sample from the KMOS Lens-Amplified Spectroscopic Survey (KLASS), Mason et al. (2019) recently have been able to place a lower limit on the average IGM neutral hydrogen fraction of > 0.76 (68 per cent), >

0.46 (95 per cent) at z ∼ 8, indicating a rapid evolution at the end of reionization. Using the quasars damping wing analysis, Davies et al. (2018) has constrained the IGM neutral fraction to be 0.6 at $z = 7.54$ and 0.48 at $z = 7.09$. A complementary similar analysis by Greig et al. (2019) has suggested that the IGM neutral fraction is about 0.2 at $z = 7.5$. On the other hand, the cosmic microwave background (CMB) observations also provide constraints on the duration of reionization, through the integrated optical depth. The *Wilkinson Microwave Anisotropy Prob* (*WMAP*; Hinshaw et al. 2013) CMB observations have previously measured an optical depth of 0.088, implying that reionization was complete by z ∼ 10. However, the much lower optical depth of 0.058 reported recently by *Planck* favors a sudden, short and late reionization by z ∼ 7 − 8. Their measurements suggest that the Universe was less than 10 per cent ionized by z ∼ 10. This shows the need for an additional probe that might break model degeneracy and provide an alternative and direct probe to the neutral fraction.

The 21 cm hyperfine line carries a wealth of information, which is promising to unravel the IGM nature and hence the

★ E-mail: tumelokholofelo@gmail.com(TM); sultanier@gmail.com(SH)
† Tombaugh Fellow.

reionization history. Many radio interferometer experiments, such as the Low Frequency Array (LOFAR; van Haarlem et al. 2013), the precision Array for probing the EoR (PAPER; Parsons et al. 2010), the Murchison Widefield Array (MWA; Bowman et al. 2013), the Giant Metrewave Radio Telescope (GMRT; Paciga et al. 2011), the Hydrogen EoR Array (HERA; DeBoer et al. 2017) and Square Kilometer Array (SKA; Mellema et al. 2013), aim to detect reionization on cosmological scales through its 21-cm fluctuations. All these experiments motivate the preparation and development of theoretical methods and statistical tools to extract possible constraints on the reionization history.

In this light, many methods have been already developed to constrain the reionization history. These include: fitting to Ly-α and optical depth measurements using Markov chain Monte Carlo (MCMC) linked to a seminumerical model (e.g. Greig et al. 2016), inferring the reionization history from parameters constraints against 21 cm mock power spectrum (e.g. Greig & Mesinger 2015), identifying H II bubbles (e.g. Giri et al. 2018) and recently using convolutional neural networks (CNNs) to constrain the reionization duration (La Plante & Ntampaka 2018). While La Plante & Ntampaka (2018) found that their designed CNN recovers the reionization duration within ∼10 per cent, their pipeline ignores the thermal noise contribution and implements a more simplified angular resolution treatment through applying a cut-off on the $k_\perp$ modes inferred from the experiment resolution.

In this work, we design a CNN to extract the neutral fraction directly from 21-cm images at each redshift, thus producing a full reionization history, which is one of the first quantities we would like to measure from 21-cm experiments. This approach relies directly on imaging and the relation between the 21-cm signal and ionized patches, without requiring to go through the derivation of the ionization fraction from power spectrum statistics, being therefore more robust to model assumptions. The images are produced by our seminumerical model SIMFAST21[1] (Santos et al. 2010). We implement a more physically motivated and realistic 21-cm noise to our 21 images, following the recipe presented in Hassan et al. (2018), that accounts for the experiment thermal noise, the angular resolution using the detailed baseline distribution as well as the effect of foregrounds. We focus our analysis on phase one of the SKA (the low-frequency part, SKA1-LOW), given its great imaging capabilities, although our approach can easily be applied to other 21cm arrays such as HERA and LOFAR. Our CNN is developed in PYTHON with the TensorFlow framework[2] (TENSORFLOW), an open-source software library for numerical computation (Abadi et al. 2016).

This paper is organized as follows: we provide a summary of the 21-cm brightness temperature semi-numerical simulations and the 21-cm noise simulations in Section 2. The designed CNN is introduced in Section 3. We present our results in Section 4, and conclude in Section 5.

2 SIMULATIONS

2.1 SIMFAST21

We use the Instantaneous version of our seminumerical model SIMFAST21 that has been developed in Hassan et al. (2016). This model has been recently shown to be in a good agreement with

predictions from our radiative transfer simulation (ARTIST; Molaro et al. 2019) in terms of the ionization morphology and 21-cm power spectrum. We describe generally the simulation ingredients, and defer to Santos et al. (2010) for the full details of the simulation algorithm, and to Hassan et al. (2016) for further updates on the Instantaneous model.

The initial step of the simulation is to generate the dark matter density from a Gaussian distribution using a Monte Carlo approach in the linear regime. Next, it dynamically evolves the density field from the linear to nonlinear regime by applying the Zel'dovich (1970) approximation. The dark matter haloes are then generated using the excursion-set formalism (ESF). Ionized regions are identified using a similar form of the ESF that is based on a comparison between the ionization rate $R_{\rm ion}$ and the recombination rate $R_{\rm rec}$ in spherical regions of decreasing sizes as specified by the ESF. Regions are flagged as ionized if

$$f_{\rm esc} R_{\rm ion} \geq R_{\rm rec}, \tag{1}$$

where $f_{\rm esc}$ is our assumed escape fraction. The $R_{\rm ion}$ parametrization is derived from a combination of the radiative transfer simulation (Finlator et al. 2015), and larger hydrodynamic simulation (Davé et al. 2013) that have both been shown to reproduce a wide range of observations, including low-redshift observations. The $R_{\rm ion}$ is parametrized as a function of halo mass $M_{\rm h}$ and redshift z as follows:

$$\frac{R_{\rm ion}}{M_{\rm h}} = 1.1 \times 10^{40} (1+z)^{D_{\rm ion}} \left(\frac{M_{\rm h}}{9.51 \times 10^7} \right)^{C_{\rm ion}}$$
$$\times \exp \left(\frac{-9.51 \times 10^7}{M_{\rm h}} \right)^{3.0}, \tag{2}$$

where the best-fitting parameters were found to be $C_{\rm ion} = 0.41$ and $D_{\rm ion} = 2.28$ (Hassan et al. 2016). Later, we will vary these parameters to generate our training data set, which quantify the ionizing emissivity dependence on halo mass and redshift. Note that equation (2) shows that $R_{\rm ion}$ scales as $M_{\rm h}^{1.41}$, which is consistent with the star formation rate−$M_{\rm h}$ relation previously found by Finlator, Davé & Özel (2011). The $R_{\rm rec}$ is obtained from the radiative transfer simulation (Finlator et al. 2015), in order to account for the clumping effects below our cell size. The $R_{\rm rec}$ is parametrized as a function of overdensity Δ and redshfit z as follows:

$$\frac{R_{\rm rec}}{V} = 9.85 \times 10^{-24} (1+z)^{5.1} \left[\frac{(\Delta/1.76)^{0.82}}{1+(\Delta/1.76)^{0.82}} \right]^4, \tag{3}$$

where V refers to the cell volume. We defer to Hassan et al. (2016) for the full details on the derivation of the $R_{\rm ion}$ and $R_{\rm rec}$ and their effects on several reionization observable. The 21 cm brightness temperature boxes are directly computed using the density and ionization fields assuming that the spin temperature is much higher than the CMB temperature, which is a valid assumption at lower redshifts, $z < 10$ (e.g. Santos et al. 2010) as considered in this work.

2.2 21-cm instrument simulation

The next step is to convert this simulation into a more realistic data set by including instrumental effects (such as noise, resolution, foreground residuals). We call these new images, the 'mock' maps. We partially follow the recipe developed in Hassan et al. (2018), particularly for the foreground cleaning. We account directly for the resolution in frequency and angular scales following the most updated documentation for the SKA-LOW configuration (Braun et al. 2017). According to the imaging sensitivity analysis performed

Table 1. Summary of our assumed SKA design.

Array design	512 stations
Station diameter, D [m]	35
Total observation time t_{int} [h]	3000
Line sensitivity [μJy beam^{-1}]	973
Map resolution [arcmin]	5
Frequency resolution [MHz]	1
Redshift	10, 9, 8 ,7, 6
Frequency [MHz]	129 , 142, 158, 178, 203
Thermal noise [mK]	1.8, 1.6, 1.4, 1.2, 1.
Default wedge slope m, equation (4)	0.27, 0.23, 0.19, 0.15

by Braun et al. (2017) in the frequency range of our interest ($z = 6$–10, $\nu = 203$–129 MHz), the line sensitivity is equal to 973 μJy beam^{-1} for a fractional bandwidth ($\Delta\nu/\nu = 10^{-4}$) and integration time $t_{int} = 1$ h. These values will be used directly in our noise pipeline to include more realistic instrumental effects following the most updated SKA-LOW design. Here, we restrict our analysis to the SKA1-LOW design, given its promising imaging capabilities and defer a more detailed comparison between different experiments, such as with HERA and LOFAR, to future work.

Using SIMFAST21, we run many large-scale reionization simulations with a box size of 500 Mpc and 200^3 cells. This box size is sufficient to capture reionization on large scales (Iliev et al. 2014). We then add a realistic SKA-like noise to these simulations using the following pipeline which consists of three parts:

(i) Foreground cleaning: Fourier modes that lie outside the so-called reionization window (i.e. inside the foreground wedge) are foreground contaminated. The foreground wedge slope m is approximately given by

$$m = \frac{D \, H_0 \, E(z) \, \sin\theta}{c(1 + z)}, \qquad (4)$$

where H_0 is the Hubble parameter, c is the speed of light, $E(z) \equiv \sqrt{\Omega_m(1 + z)^3 + \Omega_\Lambda}$, and θ is the field of view. We zero out all modes within the wedge, satisfying $k_{||} < m \, k_\perp$. For the same experiment (same beam angle), the slope (m) increases with redshift, which means more modes are removed at higher redshifts. We quote exact m values for the SKA at our redshifts of interest in Table 1. This is the first part of the noise pipeline which is applied on all 21-cm boxes to filter out the foreground wedge.

(ii) Resolution: our simulation has a frequency resolution, the slice width in z-direction, of about $\sim$0.15 MHz at $z = 8$. We choose to apply the noise on maps with frequency resolution of 1 MHz, and hence we average six successive slices along z-axis to obtain a single mock map. The angular resolution of our simulation is about $\sim$1 arcmin at $z = 8$, and we convert our maps on $x - y$ plane from 200 $\times$ 200 to 40 $\times$ 40 pixels to obtain a resolution of 5 arcmin. This step is applied on the foreground filtered box from the previous step.

(iii) Thermal noise: we use directly the line sensitivity reported by Braun et al. (2017), and then convert its value using the parameters assumed in our mock survey. We assume long integration time of 3000 h following the deep survey strategy outlined by Koopmans et al. (2015). For angular resolution of 5 arcmin, frequency resolution of 1 MHz, and integration time of 3000 h, the thermal noise is about $\sim$1 mK at $z = 6$. All values at other redshifts are quoted in Table 1. We then generate an 40 $\times$ 40 pixel map whose pixels' values are drawn from a Gaussian distribution with a zero mean and standard deviation that is set to the thermal noise value.

We then finally add the thermal noise map to the resulting map from the previous step.

Fig. 1 shows two randomly selected 21-cm images from our training samples from a box size of 500 Mpc and N = 200^3, at neutral fractions $x_{H_I} \sim 20$ per cent (top panels), and 80 per cent (bottom panels) at $z = 6$ and $z = 10$, respectively. On the right, we show the corresponding 21-cm mock images obtained using our 21-cm noise pipeline as described above. The high angular resolution of our assumed SKA design, due to the high ultraviolet-coverage, allows resolving most of the original ionized bubbles on large and small scales. In highly ionized IGM (e.g. top panels), the noise dominates the ionized regions where the 21cm signal vanishes, but nevertheless, the signal features are still clearly present. In contrast, at highly neutral IGM (e.g. bottom panels), the ionized bubbles are very small, extending to the scales where the noise has the maximum effect. In this case, the original signal features are much harder to recognize, which might be more challenging for the neural network to derive exactly the true neutral fraction.

3 CNN

CNNs have been very successful in reionization to perform parameter regression (e.g. Gillet et al. 2018; Hassan et al. 2020), classification (e.g. Hassan et al. 2018), and emulating reionization simulation (e.g. Chardin et al. 2019). CNN is a subclass of neural networks – a system of interconnected artificial neurons that exchange messages between each other. It draws its power of best performance in dealing with images by taking advantage of the spatial structure of the inputs (for a comprehensive review see Rawat et al. 2017). The basic structure of CNN consists of convolutional, pooling, and fully connected layers. Each layer is basically a linear combination of the components of the input (x) with weights and biases. Convolutional layers play the role of feature extraction from a 2D input. The role of the pooling layer is to up/down-sample the output of a convolutional layer, which basically reduces the spatial size and resolution of the features. The fully connected layers aim is the global features extraction from a 1D input. The CNN attempts to find the best set of weights and biases that minimize a specific loss function, which is the distance between the true labels and the network predictions. The minimization occurs through an optimizer that computes the loss function gradients with respect to all network parameters (weights and biases). These gradients, in principle, indicate the directions at which the network parameters can be updated so that the loss is smaller, and hence the network predictions are closer to the true expected labels. Most optimizers are variants of the stochastic gradient descent (SGD). Our network uses Huber loss (Huber 1964) as a loss function. Huber loss draws its power from combining advantages of two widely used loss functions, mean square error (MSE) and mean absolute error (MAE). It automatically turns into MAE when the error is large, and hence making it less sensitive to outliers. We use the adaptive moment estimation (Adam, Kingma & Ba 2014) as an optimizer algorithm, which is a modified SGD form. Adam adds a momentum term to the classical SGD to accelerate convergence and adapts the learning rate automatically. These features ensures fast learning, while being less sensitive to the outliers. We present the summary of the hyperparameters used in our network in Table 2.

Our best performing network is composed of three convolutional blocks and three fully connected layers. Each convolutional block contains two convolutional layers with 5 $\times$ 5 kernel size and followed by 2D max-pooling layer. Batch normalization and the
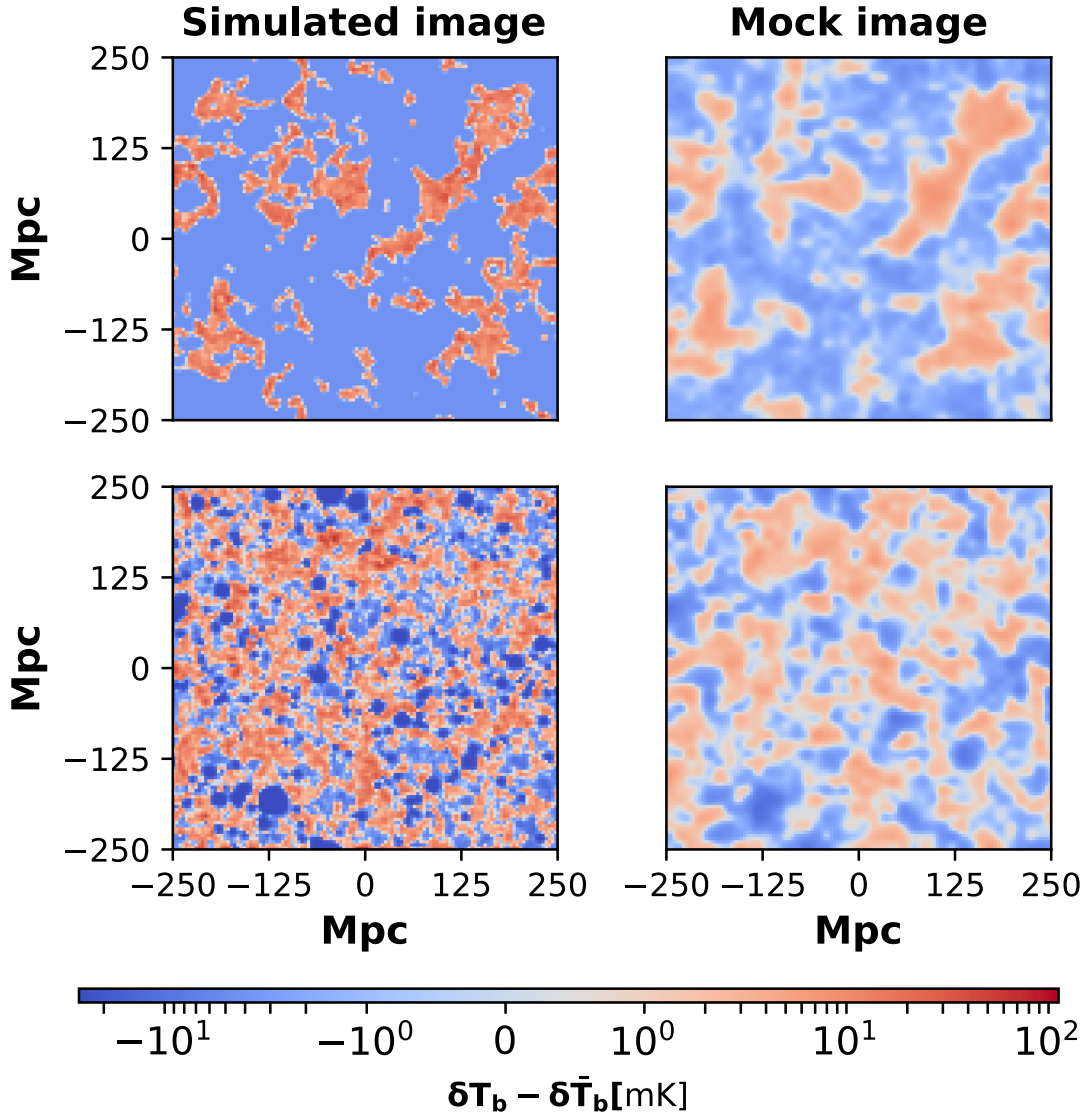
Figure 1. Example of two randomly selected 21-cm images and their mock versions, using our assumed SKA design, at $x_{\rm HI} \sim 20$ per cent (top panels) and 80 per cent (bottom panels). The mean value from each image is subtracted.

Table 2. Summary of the hyperparameters choice for the network.

Hyperparameter	Value
Learning rate	Start $=10^{-2}$
Batch-size	60
Number of epochs	300
Dropout rate	20%

rectified linear unit (ReLU) activation are applied after each layer, except the final output layer, to regularize the training process. A 20 per cent dropout rate is applied after the first fully connected layers in order to prevent overfitting. Summary of the architecture used in this work is presented in Table 3. Referring to Table 2, we train the network for a total of 300 epochs with the start learning rate of 10^{-2}.

3.1 Training data sets

Using SIMFAST21, we run 1000 reionization simulations with a box size of 500 Mpc and number of cells $N = 200^3$, which results in a resolution of 2.5 Mpc. Each realization is obtained from different realizations of the initial density field fluctuations through random change of the seed number, different set of astrophysical parameters, changing the photon escape fraction $f_{\rm esc} = (0.01–1)$, $R_{\rm ion}$-$M_{\rm h}$ power dependence $C_{\rm ion} = (0–1)$ and $R_{\rm ion}$ redshift evolution index $D_{\rm ion} = (0–2)$, and different set of cosmological parameters, changing the matter density parameter $\Omega_{\rm m} = (0.2–0.4)$, the Hubble constant $H_0 = (60–80)$, and the matter fluctuation amplitude $\sigma_8 = (0.7–0.9)$. The range considered for the astrophysical parameters is motivated from our previous MCMC estimates to match the simulation to several reionization observables (Hassan et al. 2017), and those of the cosmology is inspired by the recent parameters estimates from the Planck Collaboration VI 2018, G37. This ensures that our training sample contains very different set of 21-cm maps that accounts self-consistently for the cosmic variance. For each simulation, we generate the 21-cm brightness temperature box for

Table 3. Summary of CNN architecture used to estimate the neutral fraction from 21-cm maps for the Simulated data set. Same architecture is used for the mock data set, except the input layer dimension is 40×40.

Layer	Dimension
Input (21-cm map)	$200 \times 200 \times 1$
2D convolution	$200 \times 200 \times 8$
2D convolution	$200 \times 200 \times 8$
Batch normalization + Relu	
2D max-pooling	$100 \times 100 \times 8$
2D convolution	$100 \times 100 \times 16$
2D convolution	$100 \times 100 \times 16$
Batch normalization + Relu	
2D max-pooling	$50 \times 50 \times 16$
2D convolution	$50 \times 50 \times 32$
2D convolution	$50 \times 50 \times 32$
Batch normalization + Relu	
2D max-pooling	$25 \times 25 \times 32$
Flattening	20 000
Fully connected	200
Batch normalization + Relu	
Dropout	
Fully connected	100
Batch normalization + Relu	
Fully connected	50
Batch normalization + Relu	
Output (neutral fraction, $x_{H I}$)	1

redshifts = 10, 9, 8, 7 and, 6, which are enough to form a decent size for training purposes. Overall, we extract ∼20 000 21-cm maps in total and consider 80 per cent, 10 per cent, and 10 per cent out of this total for training, testing and validation, respectively. During the training, our data set is divided into mini-batches of size 60. Note that these 21-cm maps are labeled according to their neutral fraction, that is computed from the corresponding ionization map, instead of the globally averaged neutral fraction at each redshift. This indicates that our network aims to recover the local neutral fraction per slice by capturing the fluctuations along different directions.

4 RESULTS

We train the network on the simulated data set and then on the mock data set with the presence of the SKA instrumental effects as described earlier. We first quantify network performance in terms of the evolution of the loss, alternatively called the error rate, over training iteration in Fig. 2. We show the loss for the simulated data set with black and the mock data set with blue colour. Solid and dashed lines represent training and testing loss, respectively. In both cases (simulated or mock), we find that the network converges very quickly from the first ∼100 training epochs where the training and testing losses both become approximately constant. The fluctuations around these losses are due to the random selection of mini-batch for training and testing at each iteration. When adding the instrumental effects from SKA as seen in the mock data set, the loss value slightly increases for both training and testing. This slight loss change suggests a slight accuracy change, and hence our network design seems to be able to extract the neutral fraction information from large-scale 21-cm maps regardless the presence of SKA-like noise.
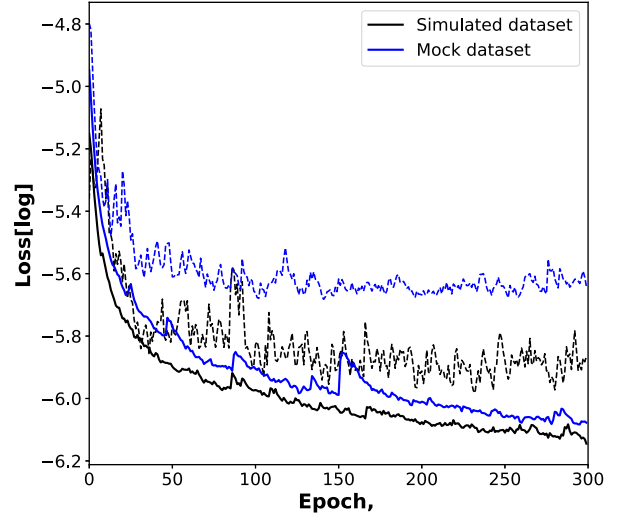

Figure 2. The loss function (error rate) evolution over training epochs for training (solid) and testing (dashed) data set without (black) and with (blue) instrumental effects from SKA. The network converges from the first 100 iterations for both training and testing with simulated data set. Adding the instrumental effects from SKA increases the loss slightly, indicating slight reduction in overall accuracy.

We further assess the network performance using the coefficient of determination R^2 and the Root MSE (RMSE) as follows:

$$R^2 = 1 - \frac{\sum(y_{predicted} - y_{true})^2}{\sum(y_{true} - \bar{y}_{true})^2}, \tag{5}$$

$$RMSE = \sqrt{\frac{1}{N}\sum(y_{predicted} - y_{true})^2}, \tag{6}$$

where the summation runs through the whole validation data set and the bar indicates the average. The R^2 quantifies the fraction by which the error variance is less than the true variance, whereas the RMSE measures the average squared error. In Fig. 3, we show the actual predictions for the neutral fraction from our designed CNN using the whole validation data set. The colour-code on the data points represents the redshifts as indicated on the right-hand side colourbar. We observe a very weak dependency of the neutral fraction on the redshift as there is no trend of colours-coded data points distribution visible (we note that we can have different neutral fractions at the same redshift since we are changing the simulations parameters). This is also seen from Table 4 where the R^2 and RMSE are approximately constant, particularly in the case for the simulated data set. For the mock data set, there seem to be a mild redshift evolution at high redshift as the RMSE drops by ∼1 order of magnitude between $z = 8$–10. This is mainly driven by the increase of the thermal noise as a function of tedshift. In both panels in the case of the simulated and mock data set, the scatter is fairly small which shows that our CNN is very successful in extracting the neutral fraction from 21-cm images with very high accuracy of $R^2 = 99$ per cent on the simulated data set. When adding the instrumental effects from our assumed SKA design, the R^2 is only reduced by 1 per cent as shown in the right-hand panel. The total RMSE in estimating the neutral fraction, for the overall bins, is 2.1×10^{-4} and 1.3×10^{-3} for the simulated and mock data sets, respectively. Similar values are found for the RMSE. This shows that our designed CNN is a robust tool to constraining the neutral fraction, and hence the reionization history from future SKA observations.
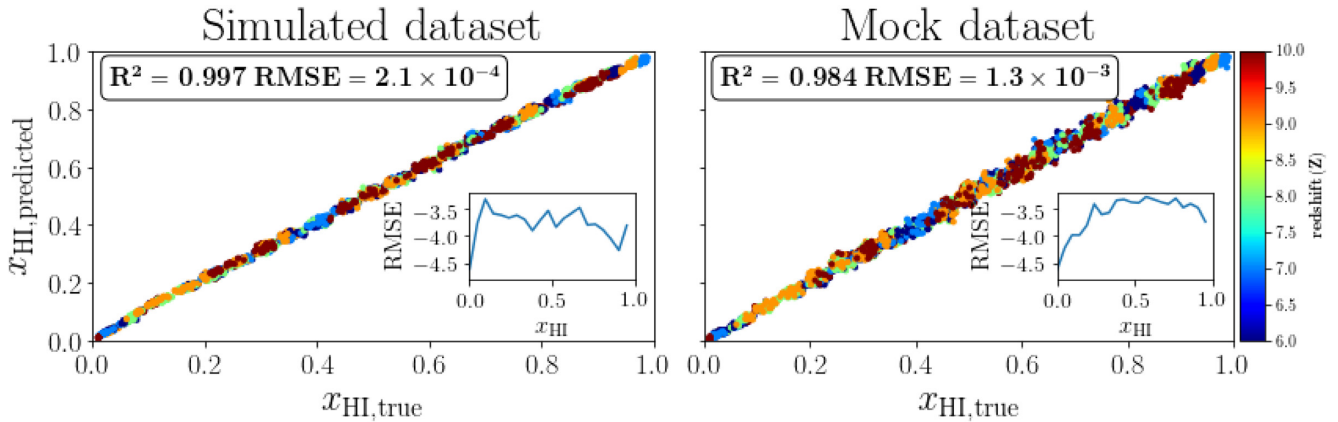
Figure 3. Relationship between the true versus predicted neutral fraction values from the CNN for the simulated data set (left-hand panel) and mock data set (right-hand panel) using the whole validation data set (circles) colour-coded with redshifts which shows a weak dependence on the redshift. The insets show the RMSE evolution as a function of the neutral fraction, indicating moderate/strong evolution in the case of the simulated/mock data set. The total R^2 and RMSE values are quoted in each plot. For both data sets, the scatter is fairly small and the CNN predictions match the true values very well. Adding the SKA instrumental effects reduces the R^2 value only by 1 per cent.

Table 4. RMSE and Coefficient of determination (R^2) for the simulated and mock validation data sets, as a function of redshift.

Redshift (z)	RMSE	R^2	$RMSE_{noise}$	R^2_{noise}
6	1.7×10^{-4}	0.998	6.4×10^{-4}	0.992
7	1.2×10^{-4}	0.997	4.5×10^{-4}	0.995
8	1.9×10^{-4}	0.998	1.1×10^{-3}	0.986
9	2.3×10^{-4}	0.997	6.8×10^{-4}	0.991
10	2.4×10^{-4}	0.997	3.7×10^{-3}	0.955

We next explore the neutral fraction recovery dependence on neutral fraction by computing the RMSE evolution for all neutral fraction bins as depicted in the insets in Fig. 3. We find a strong evolution of the RMSE as a function of neutral fraction. The RMSE increases with increasing neutral fraction, indicating a harder parameter recovery. This is expected since the noise contaminates the signal more effectively at high neutral fraction values as seen in Fig. 1, where the ionized bubbles are very small. While no dependence on redshift is seen, it is known that the low neutral fraction IGM only exists at the end of reionization at $z \sim 7$ and 8. This shows that such a technique is very efficient to constraining the neutral fraction at low redshifts when the signal is low (due to low neutral fractions).

We finally attempt to understand how CNN is able to create the link between the input (21-cm image) and the output (neutral fraction). We do so by looking at the response of the first convolutional layer at the final training step. As the images go deeper in the network (to the second and third layers), it becomes more difficult to visualize these images since some information will be lost and some transformation will occur, and hence we restrict the visualization to the first convolutional layer. In this first layer, we have a set of eight weights, and we show the convolution of a random 21-cm image to these weights in Fig. 4. We find that the activation of the ionized bubbles is relatively similar, although the bubbles edges are somewhat fainter with some weights. However, these trained weights do activate the neutral regions of the 21-cm image very differently as shown by the red colour, indicating that the network is using these variations to estimate the neutral fraction out of the input 21-cm map.

5 CONCLUSIONS

In this work, we have designed a CNN that is able to read out the neutral fraction from 21-cm images, generated from our semi-numerical simulation (SIMFAST21), with a very high accuracy $R^2 = 99$ per cent and RMSE $= 2.1 \times 10^{-4}$ (see Fig. 3). We have also considered the proposed SKA1-LOW array configuration to add realistic instrumental effects that account for the thermal noise, angular resolution and foreground contamination. We have shown that adding the SKA instrumental effects to the simulated 21-cm images slightly delays the training process (see Fig. 2), but nevertheless the network is still able to extract the neutral fraction with a similarly high accuracy $R^2 = 98$ per cent and RMSE $= 1.3 \times 10^{-3}$, which is only 1 per cent less than the accuracy without the presence of noise from the SKA (see Fig. 3). The accuracy depends weakly on redshift, but increases rapidly with decreasing neutral fraction. This is due to the fact that the instrumental noise increases towards high redshift where the Universe is highly neutral. The designed network activates the neutral regions in the 21-cm images differently (see Fig. 4) which illustrates how the network creates the mapping between the input 21-cm image and the output neutral fraction.

Our results are limited to the approximation and assumptions used in the 21-cm instrument simulations. A more refined recipe to account for the instrumental effects, particularly the foreground cleaning method, might alter our conclusion. The approximation implemented in the seminumerical simulations place an additional limitation to the presented results.

The designed network shows the ability of machine learning to constrain the reionization history from 21-cm tomography with future EoR experiments. This approach is completely model independent as it relies on connecting directly images to ionization fractions. The huge number of maps in the training data set ($\sim$20 000) was very helpful to obtain such a high accuracy with/without the presence of instrumental effects from SKA. While we only focused on the SKA design, our analysis can be easily extended to include other experiments such as HERA and LOFAR, although the large noise and/or low resolution might create extra challenges. We leave for future work to present a detailed comparison between the ability of different 21-cm arrays to constrain the reionization history. Our results also show that the foreground cleaning does not prevent the designed network to achieve very high accuracy. This is in contrast to previous results in Hassan et al. (2018), where the foreground
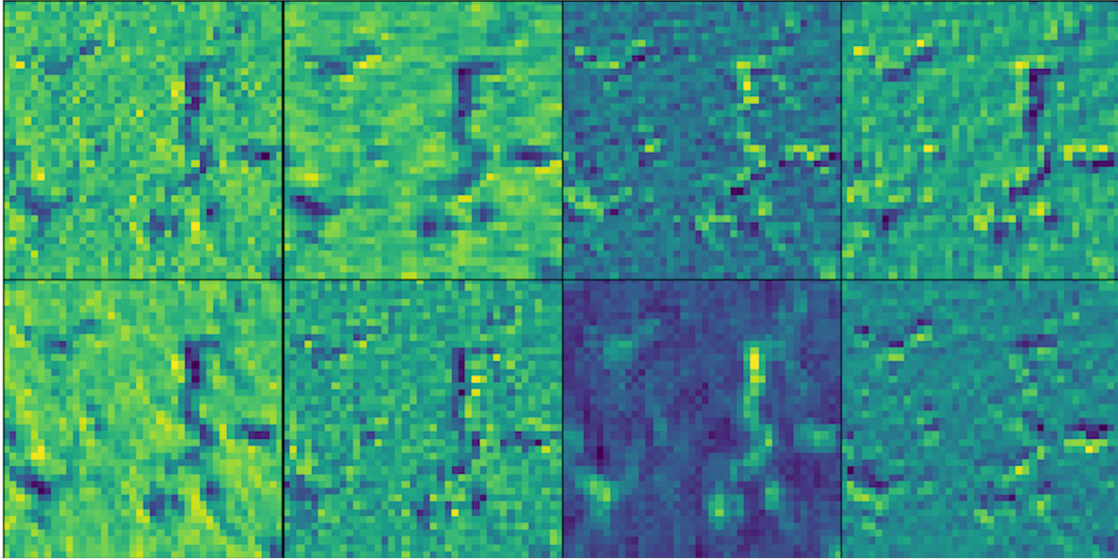
Figure 4. The response of convolving a randomly selected 21-cm map with the trained set of eight weights of the first convolutional layer before the application of the ReLU. The weights activate the input map differently, particularly, the neutral region. The ionized bubble activation appears to be approximately similar, albeit fainter with some weights. These variations are used in the network to estimate the neutral fraction out of the 21-cm map.

cleaning can present a significant challenge to classify between galaxies and active galactic nucleus reionization models, even for a highly sensitive 21-cm array such as the SKA. In future work, we plan to check the network ability to constrain the reionization history from the 3D 21 cm signal light cone, which contains more information than the static 21-cm images used in this study.

REFERENCES

Abadi M., 2016, preprint (arXiv:1603.04467)
Becker G. D., Bolton J. S., Madau P., Pettini M., Ryan-Weber E. V., Venemans B. P., 2015, MNRAS, 447, 3402
Bowman J. D. et al., 2013, PASA, 30, 31
Braun R., et al., 2017, SKA-TEL-SKO-0000818. https://astronomers.skatel escope.org/, 20-Jan-2020
Chardin et al., 2019, MNRAs, 490, 1055
Davé R., Katz N., Oppenheimer B. D., Kollmeier J. A., Weinberg D. H., 2013, MNRAS, 434, 2645
Davies et al., 2018, ApJ, 864, 142
DeBoer D. R. et al., 2017, PASP, 129, 974
Fan X., Carilli C. L., Keating B., 2006, ARA&A, 44, 415
Finlator K., Davé R., Özel F., 2011, AJ, 743, 169
Finlator K., Thompson R., Huang S., Davé R., Zackrisson E., Oppenheimer B. D., 2015, MNRAS, 447, 2526
Gillet N. et al., 2018, MNRAS, 484, 282
Giri, Sambit K., Garrelt M., Ghara R., 2018, MNRAS, 479, 5596
Greig B., Mesinger A., 2015, MNRAS, 449, 4246
Greig B., Mesinger A., 2016, MNRAS, 465, 4838
Greig B. et al., 2019, MNRAS, 484, 5094
Hassan S., Davé R., Finlator K., Santos M. G., 2016, MNRAS, 457, 1550
Hassan S., Davé R., Finlator K., Santos M. G., 2017, MNRAS, 468, 122
Hassan S., Liu A., Kohn S., La Plante P., 2018, MNRAS, 483, 2524
Hassan S. et al., 2020, preprint (arXiv:1907.07787)
Hinshaw et al., 2013, AJ, 208, 19
Huber P. J., 1964, Ann. Math. Statist., 35, 73
Iliev et al., 2014, MNRAS, 439, 725
Kingma D. P., Ba J., 2014, preprint (arXiv:1412.6980)
Koopmans et al., 2015, Advancing Astrophysics with the Square Kilometre Array (AASKA14). Proc. Science, 2015
La Plante P., , Ntampaka M., 2018, ApJ, 880(2), 110
Loeb A., Barkana R., 2001, ARA&A, 39, 19
Mason C. A., et al., 2019, MNRAS, 485, 3947
Mellema et al., 2013, Exp. Astron., 36, 235
Molaro M., Davé R., Hassan S., Santos M. G., Finlator K., 2019, MNRAS, 489, 5594
Paciga G. et al., 2011, MNRAS, 413, 1174
Parsons A. R. et al., 2010, AJ, 139, 1468
Planck Collaboration VI, 2018, preprint (arXiv:1807.06209)
Rawat W., Wang Z., 2017, Neural Comput., 29, 2352
Santos M.G., Ferramacho L., Silva M. B., Amblard A., Cooray A., 2010, MNRAS, 406, 2421
van Haarlem M. P. et al., 2013, A&A, 556, A2
Zel'dovich Y. B. et al., 1970, A&A, 5, 84

This paper has been typeset from a TEX/LATEX file prepared by the author.